LETTER TO THE EDITOR

A transiting exocomet detected in broadband light by TESS in the β Pictoris system

S. Zieba¹, K. Zwintz¹, M. Kenworthy², and G. M. Kennedy³

- Universität Innsbruck, Institut für Astro- und Teilchenphysik, Technikerstraße 25, A-6020 Innsbruck e-mail: konstanze.zwintz@uibk.ac.at
- Leiden Observatory, Leiden University, P.O. Box 9513, 2300 RA Leiden, The Netherlands
- Department of Physics, University of Warwick, Gibbet Hill Road, Coventry CV4 7AL, UK

ABSTRACT

Aims. We search for signs of falling evaporating bodies (FEBs, also known as exocomets) in photometric time series obtained for β Pictoris after fitting and removing its δ Scuti type pulsation frequencies.

Methods. Using photometric data obtained by the TESS satellite we determine the pulsational properties of the exoplanet host star β Pictoris through frequency analysis. We then prewhiten the 54 identified δ Scuti p-modes and investigate the residual photometric

Results. We identify three distinct dipping events in the light curve of β Pictoris over a 105-day period. These dips have depths from 0.5 to 2 millimagnitudes and durations of up to 2 days for the largest dip. These dips are asymmetric in nature and are consistent with a model of an evaporating comet with an extended tail crossing the disk of the star.

Conclusions. We present the first broadband detections of exocomets crossing the disk of β Pictoris, consistent with the predictions made 20 years earlier by Lecavelier Des Etangs et al. (1999). No periodic transits are seen in this time series. These observations confirm the spectroscopic detection of exocomets in Calcium H and K lines that have been seen in high resolution spectroscopy.

Key words. Comets: general – Stars: planetary systems – Stars: individual: β Pictoris – Techniques: photometric – circumstellar

Alms. We search for signs of falling evaporating bodies (FEBs, als Pictoris after fitting and removing its δ Scuti type pulsation frequent Methods. Using photometric data obtained by the TESS satellite β Pictoris through frequency analysis. We then prewhiten the 54 ic time series for the presence of FEBs.

Results. We identify three distinct dipping events in the light curve 0.5 to 2 millimagnitudes and durations of up to 2 days for the large a model of an evaporating comet with an extended tail crossing the Conclusions. We present the first broadband detections of exocom made 20 years earlier by Lecavelier Des Etangs et al. (1999). No confirm the spectroscopic detection of exocomets in Calcium H an Key words. Comets: general – Stars: planetary systems – Stars: matter

1. Introduction

Our voyage of extrasolar planetary system discovery and exploration arguably began with the image of β Pictoris' circumstellar disk (Smith & Terrile 1984), which showed that the infrared excesses discovered by IRAS (e.g. Aumann et al. 1984) were not "shells", but disks on scales similar to the extent of our Solar system.

β Pictoris (HD 39060) is one of the brightest stars in the sky (V = 3.86 mag) lying at a distance of only 19.76 pc (Brown et al. 2018). It is a member of the β Pictoris moving group with an age of ~23 Myr (Mamajek & Bell 2014). β Pictoris harbors a warped debris disk composed of dust and gas which is seen nearly edgeon and has an outer extent ranging from 1450 to 1835 AU (Larwood & Kalas 2001). In 2010, the planet β Pictoris b was detected using VLT/NaCo observations by Lagrange et al. (2010). Because of its close proximity and circumstellar disk, the β Pictoris system can be considered an ideal test bed to study the formation and evolution of planetary systems, including minor bodies such as exocomets and exomoons. Indeed, the first re-

formation and evolution of planetary systems, including minor bodies such as exocomets and exomoons. Indeed, the first reports of comets around stars other than our Sun came from spectroscopic observations of the β Pictoris system, which identified transient absorption features that change in time (Ferlet et al. 1987; Kiefer et al. 2014b). Similar detections have also been made towards other stars, e.g., HD 172555 (Kiefer et al. 2014a). Models based on these detections included cometary comae and place the exocomets at distances of a few to several tens of stellar radii, which was confirmed by their observed acceleration (Beust et al. 1990; Kennedy 2018). Subsequent work theoreti-

cally predicted that occultations of the stellar light by these exocomets could be detected in broad-band photometric time series. Lecavelier Des Etangs et al. (1999) estimated that the depths of such signals would be of the order of tenths of a percent in flux and suggested the detection of an exocomet passage in front of β Pictoris in observations from 1981.

To date just a few stars show photometric transits consistent with the predictions. Rappaport et al. (2019) searched for dimming events in Kepler data which are potentially caused by exocomets and identified them around the two stars KIC 3542116 and KIC 11084727. A recent study by Kennedy et al. (2019) describes an algorithm to identify transit features with an ingress that is more rapid than the egress, i.e., such as expected for exocometary bodies with a long tail. The unique, deep and irregular events of dimming of the light observed from KIC 8462852 using the Kepler space telescope (Boyajian et al. 2016) was recently explained using a comet family model (Wyatt et al. 2018). The common properties of all reported events and the predictions from theoretical models (Lecavelier Des Etangs et al. 1999) have an asymmetric shape with a steep initial drop in flux and a longer tail.

In this letter we present observations of β Pictoris from TESS and show that the duration and depth of a dipping event in Sector 6 is consistent with the transit of an exocomet and agrees with the predictions made by Lecavelier Des Etangs et al. (1999).

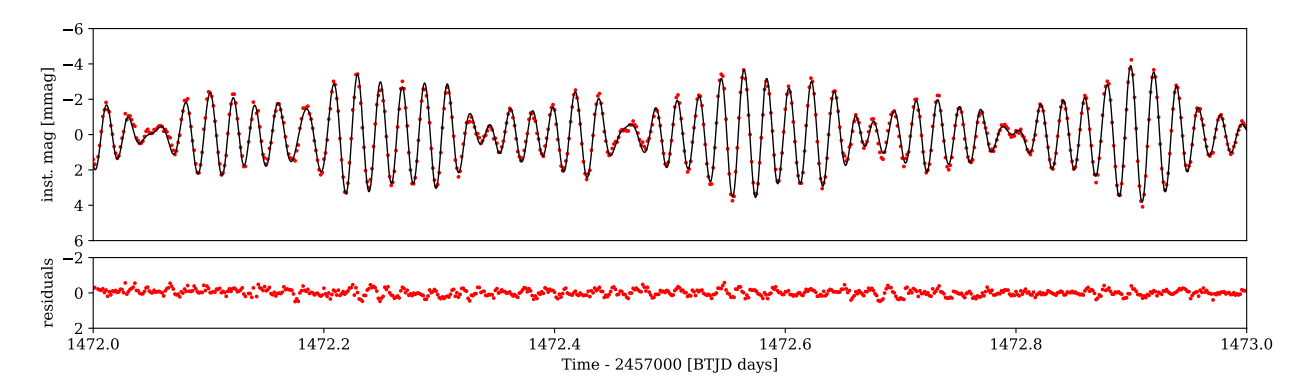


Fig. 1. A one-day zoom into the β Pictoris light curve: *upper panel*: TESS photometric time series (red points) and multi-sine fit using the 54 identified δ Scuti frequencies; *lower panel*: Residual time series after subtracting the multi-sine fit using all 54 identified pulsation frequencies.

2. Observations

We use data collected by the Transiting Exoplanet Survey Satellite (TESS; Ricker et al. 2015) from 19 October 2018 to 1 February 2019 in Sectors 4 through 7. This leads to a baseline of about 105 days with a duty cycle of 85% for the four sectors. β Pictoris (TIC 270577175, T = 3.82 mag) is one of the preselected targets for which "short cadence" 2-minute data is provided. We investigated the instrumental behaviour of TESS during the β Pictoris observations in detail to exclude any systematic effects or instrumental artefacts. A detailed description is given in the Appendix.

2.1. Fitting the stellar pulsations of Beta Pictoris

 β Pictoris is known to show δ Scuti like pulsations (Koen 2003; Koen et al. 2003; Mékarnia et al. 2017; Zwintz et al. 2019) which we need to fit and remove in order to search for signs of exocomets. Therefore, we conduct a frequency analysis using the software package Period04 (Lenz & Breger 2005) and extract all pulsation frequencies down to a signal-to-noise ratio of 4 following Breger et al. (1993). From this, we identify 54 significant p-modes in the frequency range from 23 and $76 \,\mathrm{d}^{-1}$. A one-day zoom into the light curve illustrating the pulsational behaviour is shown in the upper panel of Figure 1. A detailed description, the full list of frequencies (see Table B.1) and the corresponding amplitude spectrum (see Figure B.1) are provided in the Appendix. We subtract the multi-sine fit using the 54 frequencies, amplitudes and phases from the original TESS light curve and investigate the residuals (bottom panel in Figure 1) for the presence of FEBs.

3. Results

3.1. Exocomet transit modeling

The pulsation removed light curve shows three notable transit features, as highlighted in Figure 2. All three transits show a triangular or sawtooth shape, with a steep increase of absorption followed by an exponential decay back to the full flux level of the star. The three transits have different shapes and are not periodic. Assuming a circular orbit with period P > 105 days, and with a mass of $1.80 M_{\odot}$ for β Pictoris (Wang et al. 2016), leads to a minimum orbital radius of about 0.5 AU. It almost certain that the comet orbits are highly eccentric, so this non-periodicity is not particularly surprising.

Lecavelier Des Etangs et al. (1999) carried out a comprehensive modelling study of exocomet light curves that includes

modeling of the tail ejecta and its particle size distribution and the subsequent acceleration due to radiation pressure from the star, for different distributions of the sizes of the ejected particles. Not knowing the geometry of the exocomet orbit leads to degeneracies in the possible range of particle distributions and orbital parameters, so in this Letter we adopt a simpler one dimensional model as used in Brogi et al. (2012). While that model was designed with a transiting planet in mind, the only practical difference here is that the orbital period and eccentricity are largely unconstrained. We therefore assume a circular orbit with period P for the modelling, but report the results in terms of the transverse velocity v_{trans} of the comet across the face of the star. Adopting the nomenclature of Brogi et al. (2012), the star is modeled as a limb-darkened circular disk with radius $R_* = 1.53R_{\odot}$ (Wang et al. 2016) and linear limb darkening coefficient u = 0.275 for β Pictoris (Claret 2000).

The exocomet is assumed to be optically thin, and its extinction cross-section ρ is expressed in units of stellar area. The model has a hard front edge, and the cross-section then drops exponentially behind the comet with normalisation constant c_e and an exponential factor λ so that $\rho(\Delta\theta)=c_e e^{-\lambda(\Delta\theta)}$ with $\Delta\theta$ the angle between the comet and a point on the circular orbit of the comet. The characteristic length of the tail is therefore $1/\lambda$. The total extinction of the star is the convolution of ρ with the intensity of the occulted stellar disk and the intensity I of the star is

$$I(\theta) = 1 - \int_0^{2\pi} \rho(\theta - \theta') i(\theta', \hat{r}_c) \, d\theta'$$

where the phase angle of the orbit θ is related to the time t by $\theta = 2\pi(t - t_{mid})/P$ where t_{mid} and P are two of the five free parameters in our fit, the remaining three are b, λ and c_e . The intensity of the occulted stellar disk is:

$$i(\theta',\hat{r}_c) = 1 - u \left[1 - \frac{a}{R_*} \sqrt{\sin^2(\hat{r}_c/2) - \sin^2\theta'} \right]$$

The angular size of the chord as seen from the comet $\hat{r}_c = \arcsin(r_c/2a)$, and the chord length r_c on the star for an impact parameter $b = [1 - (r_c/2R_*)]^{1/2}$.

With these parameters the model is underconstrained, in that transits with more rapid ingress at large b (shorter transit chords) are compensated for by longer orbital periods and shorter comet tails, thus yielding the same ingress/egress slope in the model light curve. Fixing b = 0 constrains P and λ , although if the

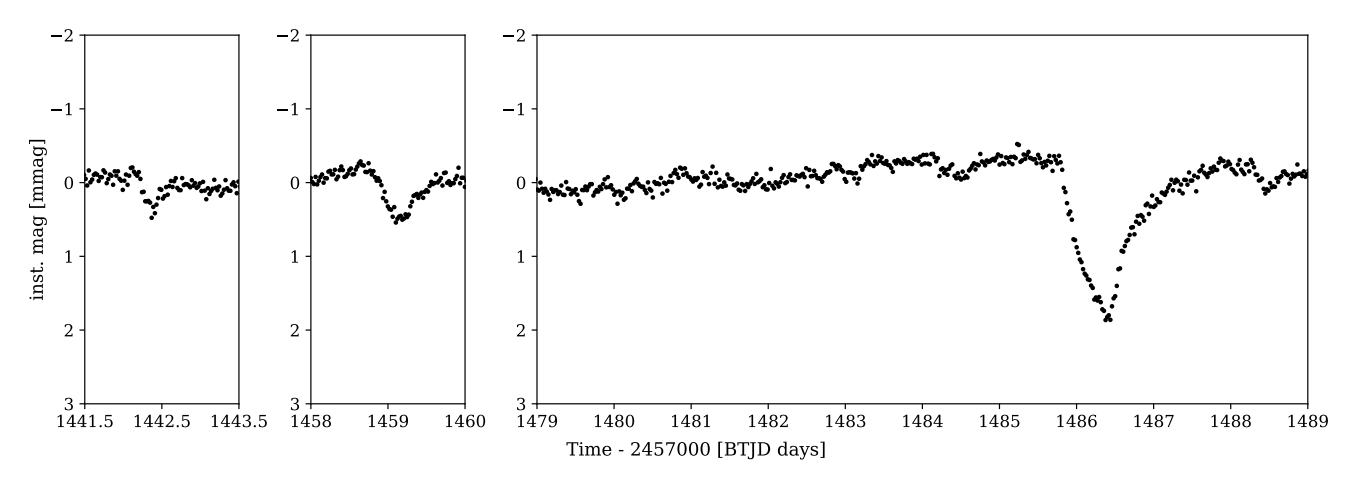


Fig. 2. Zoom-in to the three events (from left to right: transit C, B and A) in the 30-minutes binned light curve after subtraction of the pulsational signal.

Table 1. Fitted parameters from the MCMC routine with b = 0.

Parameter	Value
t_{mid}	1486.290 ± 0.001 d
b	0 (assumed)
c_e	$(3.67 \pm 0.04) \times 10^{-3}$
$1/\lambda$	$(1.22 \pm 0.04) \times 10^{-3} \text{ rad}$
v_{trans}	$19.6 \pm 0.1 \; \text{km s}^{-1}$

comet were not assumed to have a hard front edge these would again be degenerate.

We use the Python software package emcee (Foreman-Mackey et al. 2013) to perform a Markov Chain Monte Carlo (MCMC) fit to the binned light curve around the largest transit feature. We average the photometry over 30 minute bins, and calculate the error bars on the binned photometry by determining the root mean square of each set of photometric points and dividing by the square root of the number of points per bin. The photometric light curve and the best-fit model is shown for b=0 in Figure 3, along with the residuals of the fit in the lower panel. The resultant triangle plot showing the parameter distributions and correlations between the variables is shown in Figure 4. The $\pm 1\sigma$ errors of the parameters are computed by measuring the interval between 16% and 84% of the merged distribution, and the best fit values and their uncertainties are listed in Table 1.

4. Discussion

As noted above, the comet orbit is not constrained because the chord across the star is unknown, yielding a near-total degeneracy between b, λ and v_{trans} (which is derived from P). By setting b=0 the transverse velocity is constrained (for our assumption of a hard front edge for the comet), with a value of $v_{trans}=19.6~{\rm km~s^{-1}}$ (i.e. equivalent to the circular velocity at about 3 AU). Given that the radial velocities of the comets detected in calcium absorption are typically tens to hundreds of km s⁻¹, the transverse velocity seems broadly consistent with a comet on a high eccentricity orbit at a distance that is probably significantly closer to the star than 3 AU. The characteristic tail length $1/\lambda$ is small. However, as with the velocity this is also a transverse length, and in addition the physical size depends on the distance to the star. If we assume 1 AU, then this length is

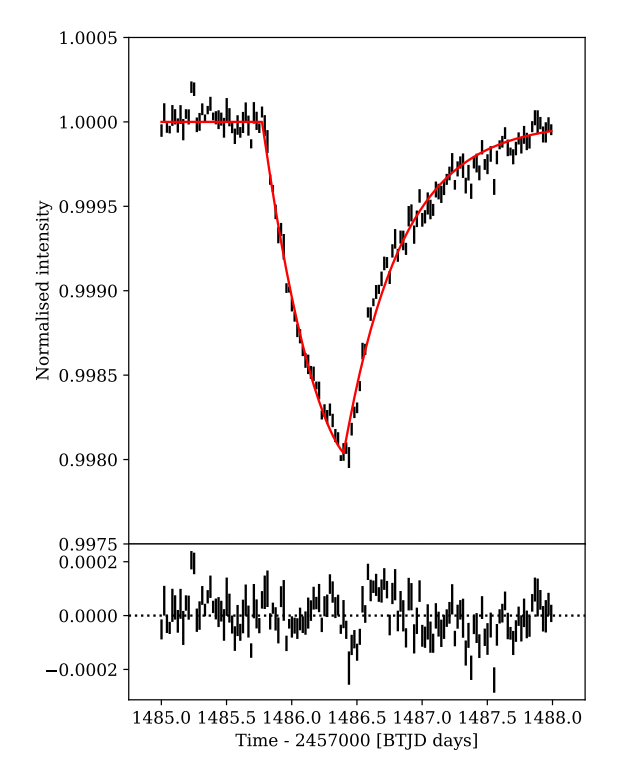


Fig. 3. Best-fit comet model. Top panel: The binned photometry showing the largest transit event. The vertical dashes are the error bars on the photometry. The red line shows the best fit model for b=0 (i.e. the median of the parameters shown in Fig. 4). The lower panel shows the residuals from the fit.

 \sim 2 × 10⁸ km, or about a tenth of the stellar diameter, indicating that most of the dust is concentrated near the comet nucleus. The close match of the data with the models of Lecavelier Des Etangs et al. (1999) suggests that those physical models are a reasonable starting point to futher interpret these data.

We chose not to include forward scattering for our exocomet model, even though Lecavelier Des Etangs et al. (1999) and others include it in their models. Our hesitation is that the long term variation in the flux of β Pictoris over Sector 6 seems to not ex-

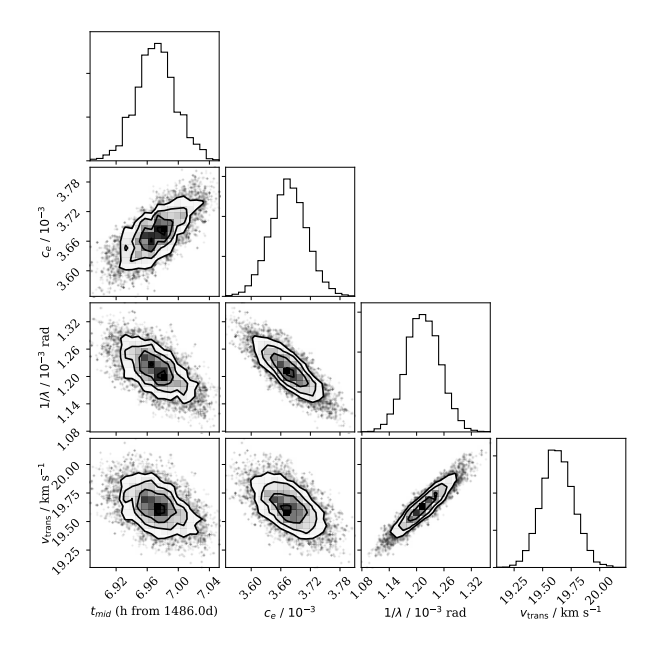


Fig. 4. Posterior probability distributions for the exocomet model with b = 0. Diagonal panels show the 1-D distributions, and the other panels show the 2-D distributions and illustrate the parameter degeneracies (primarily between transverse velocity and comet tail length).

tend or be seen in the adjacent sectors. An initial examination suggests that there is a long lived forward scattering halo associated with transit A (illustrated in the rightmost panel of Figure 2), but it is not centred on the transit itself. Forward scattering peaks are seen in transit B and C, but since these transits are at much smaller significance than transit A, there will be a much larger degeneracy in the model fitting for these two dips, and exploring whether these dips have a common orbital connection with transit A is left to a future paper.

5. Conclusions

We report the first photometric broadband detection of an exocomet transit in the β Pictoris system, consistent with the prediction of Lecavelier Des Etangs et al. (1999). We fit a simple cometary tail model to the largest of these events, seen at BTJD 1486.4, and find that it is consistent with an exponentially decaying optical depth tail convolved with the limb darkened disk of the star.

Future work includes a more comprehensive modeling of all the transits seen in the TESS light curve, and seeing if high resolution spectral observations were taken simultaneously with this transit to confirm the cometary hypothesis. A comprehensive photometric campaign was conducted during the Hill sphere transit of β Pictoris b (Kenworthy 2017) that includes bRing (Stuik et al. 2017), ASTEP (Guillot et al. 2015; Abe et al. 2013; Mékarnia et al. 2017) and BRITE-Constellation (Weiss et al. 2014) photometry. Searching this data may yield more candidate broadband transits.

A dedicated cubesat mission to monitor β Pictoris, similar to the PICSAT project (Nowak et al. 2016, 2018) would uncover more of these events, and photometry at different wavebands would help determine the size distribution of the tail particles (Lecavelier Des Etangs et al. 1999).

Acknowledgements. This paper includes data collected by the TESS mission, which are publicly available from the Mikulski Archive for Space Telescopes (MAST). Funding for the TESS mission is provided by the NASA Explorer Program. This work has made use of data from the European Space Agency (ESA) mission Gaia (https://www.cosmos.esa.int/gaia), processed by the Gaia Data Processing and Analysis Consortium (DPAC, https://www. cosmos.esa.int/web/gaia/dpac/consortium). Funding for the DPAC has been provided by national institutions, in particular the institutions participating in the Gaia Multilateral Agreement. GMK is supported by the Royal Society as a Royal Society University Research Fellow. We made use of the software package Period04 (Lenz & Breger 2005), the Python programming language (Rossum 1995) and the open-source Python packages numpy (van der Walt et al. 2011), matplotlib (Hunter 2007), astropy (Astropy Collaboration et al. 2013), lightkurve (Barentsen et al. 2019) and emcee (Foreman-Mackey et al. 2013). An online repository with materials used in this work is available at https://github.com/sebastian-zieba/betaPic_comet.

References

Abe, L., Gonçalves, I., Agabi, A., et al. 2013, A&A, 553, A49 Astropy Collaboration, Robitaille, T. P., Tollerud, E. J., et al. 2013, A&A, 558, A33

Aumann, H. H., Beichman, C. A., Gillett, F. C., et al. 1984, ApJ, 278, L23Barentsen, G., Hedges, C. L., De Mirand a Cardoso, J. V., et al. 2019, in American Astronomical Society Meeting Abstracts, Vol. 233, American Astronom-

ical Society Meeting Abstracts #233, 109.08 Beust, H., Lagrange-Henri, A. M., Madjar, A. V., & Ferlet, R. 1990, A&A, 236,

202 Boyajian, T. S., LaCourse, D. M., Rappaport, S. A., et al. 2016, MNRAS, 457,

Breger, M., Stich, J., Garrido, R., et al. 1993, A&A, 271, 482

Brogi, M., Keller, C. U., de Juan Ovelar, M. and Kenworthy, M. A., et al. 2012, A&A, 545, L5

Brown, A. G. A., Vallenari, A., Prusti, T., et al. 2018, A&A, 616, A1 Claret, A. 2000, A&A, 363, 1081

Ferlet, R., Hobbs, L. M., & Madjar, A. V. 1987, A&A, 185, 267

Foreman-Mackey, D., Hogg, D. W., Lang, D., & Goodman, J. 2013, PASP, 125, 306

Gaia Collaboration, Prusti, T., de Bruijne, J. H. J., et al. 2016, A&A, 595, A1 Guillot, T., Abe, L., Agabi, A., et al. 2015, Astronomische Nachrichten, 336, 638 Hunter, J. D. 2007, Computing In Science & Engineering, 9, 90

Jenkins, J. M. 2017, Kepler Data Processing Handbook: Overview of the Science Operations Center, Tech. rep., NASA Ames Research Center

Jenkins, J. M., Caldwell, D. A., Chandrasekaran, H., et al. 2010, ApJ, 713, L87
Jenkins, J. M., Twicken, J. D., McCauliff, S., et al. 2016, in Society of Photo-Optical Instrumentation Engineers (SPIE) Conference Series, Vol. 9913, Software and Cyberinfrastructure for Astronomy IV, 99133E

Kennedy, G. M. 2018, MNRAS, 479, 1997

Kennedy, G. M., Hope, G., Hodgkin, S. T., & Wyatt, M. C. 2019, MNRAS, 482, 5587

Kenworthy, M. 2017, Nature Astronomy, 1, 0099

Kiefer, F., Lecavelier des Etangs, A., Augereau, J.-C., et al. 2014a, A&A, 561, L10

Kiefer, F., Lecavelier des Etangs, A., Boissier, J., et al. 2014b, Nature, 514, 462 Koen, C. 2003, MNRAS, 341, 1385

Koen, C., Balona, L. A., Khadaroo, K., et al. 2003, MNRAS, 344, 1250

Lagrange, A.-M., Bonnefoy, M., Chauvin, G., et al. 2010, Science, 329, 57

Larwood, J. D. & Kalas, P. G. 2001, MNRAS, 323, 402

Lecavelier Des Etangs, A., Vidal-Madjar, A., & Ferlet, R. 1999, A&A, 343, 916 Lenz, P. & Breger, M. 2005, Communications in Asteroseismology, 146, 53 Mamajek, E. E. & Bell, C. P. M. 2014, MNRAS, 445, 2169

Mékarnia, D., Chapellier, E., Guillot, T., et al. 2017, A&A, 608, L6

Montgomery, M. H. & Odonoghue, D. 1999, Delta Scuti Star Newsletter, 13, 28 Nowak, M., Lacour, S., Crouzier, A., et al. 2018, in Society of Photo-Optical Instrumentation Engineers (SPIE) Conference Series, Vol. 10698, Space Telescopes and Instrumentation 2018: Optical, Infrared, and Millimeter Wave, 1069821

Nowak, M., Lacour, S., Lapeyrère, V., et al. 2016, in Society of Photo-Optical Instrumentation Engineers (SPIE) Conference Series, Vol. 9904, Space Telescopes and Instrumentation 2016: Optical, Infrared, and Millimeter Wave, 99044L

Rappaport, S., Zhou, G., Vanderburg, A., et al. 2019, MNRAS, 485, 2681 Ricker, G. R., Winn, J. N., Vanderspek, R., et al. 2015, Journal of Astronomical Telescopes, Instruments, and Systems, 1, 014003

Rossum, G. 1995, Python Reference Manual, Tech. rep., Centrum voor Wiskunde en Informatica (CWI), Amsterdam, The Netherlands, The Netherlands

Smith, B. A. & Terrile, R. J. 1984, Science, 226, 1421

Smith, J. C., Stumpe, M. C., Van Cleve, J. E., et al. 2012, Publications of the Astronomical Society of the Pacific, 124, 1000

Stassun, K. G., Oelkers, R. J., Pepper, J., et al. 2018, AJ, 156, 102

Stuik, R., Bailey, J. I., Dorval, P., et al. 2017, A&A, 607, A45

Stumpe, M. C., Smith, J. C., Van Cleve, J. E., et al. 2012, Publications of the Astronomical Society of the Pacific, 124, 985

van der Walt, S., Colbert, S. C., & Varoquaux, G. 2011, Computing in Science & Engineering, 13, 22

Wang, J. J., Graham, J. R., Pueyo, L., et al. 2016, AJ, 152, 97

Weiss, W. W., Rucinski, S. M., Moffat, A. F. J., et al. 2014, PASP, 126, 573

Wyatt, M. C., van Lieshout, R., Kennedy, G. M., & Boyajian, T. S. 2018, MN-RAS, 473, 5286

Zwintz, K., Reese, D. R., Neiner, C., et al. 2019, A&A submitted

Appendix A: Instrumental Behaviour

Appendix A.1: TESS photometric time series

 β Pictoris (TIC 270577175, T = 3.82 mag) is one of the preselected targets for which "short cadence" 2-minute data is provided. This Candidate Target List (CTL) is a subset of the TESS Input Catalogue¹ (TIC; Stassun et al. 2018) with about 200 000 targets for TESS 2-minute cadence observations, which were primarily chosen in order to maximize the yield of transiting exoplanets.

Figure A.1 shows the complete TESS β Pictoris light curve. The beginnings of each sector are marked with a vertical red line. The visible gaps are related to the data downlink at the perigee of TESS' orbit which occurs every 13.7 days and during which TESS halts its observations for about one day. β Pictoris was observed with CCD 1 of Camera 4 during Sector 4, with CCD 4 of Camera 3 during Sector 5 and with CCD 3 of Camera 3 during Sectors 6 and 7.

As the angle between the boresight of these cameras and both the Earth and the Moon was never smaller than 37°, we do not expect strong features created by scattered light from these two bodies during these observations.

We use the 2-minute Presearch Data Conditioning (PDC; Smith et al. 2012; Stumpe et al. 2012) light curve from the Science Processing Operations Center (SPOC) pipeline (Jenkins et al. 2016; Jenkins 2017), which was originally developed for the Kepler mission (Jenkins et al. 2010). These light curves are corrected for systematics by the SPOC pipeline. During the "momentum dumps" (i.e., thruster firings that reduce the speed of the reaction wheels and decrease the pointing jitter), TESS loses the fine attitude control mode for about 15 minutes (see the TESS Instrument Handbook²). Consequently, the pointing is less stable during these particular times, resulting in potential changes in the photometric fluxes of the target stars. Momentum dumps took place every ≈2.5 days in Sector 4, every three days in Sector 5 and every 3.125 days in Sector 6 and 7 (red triangles in Figure A.1). We omit data collected in the vicinity of "momentum dumps" in the subsequent analysis.

The data products were accessed and modified with the python package lightkurve (Barentsen et al. 2019), which retrieves the data from the MAST archive³. We remove every measurement with a non-zero "quality" flag (see §9 in the TESS Science Data Products Description Document⁴) which

mark anomalies like cosmic ray events or instrumental issues. Three days between BTJD 1421 and BTJD 1424 are removed due to higher than normal rates of spacecraft jitter. This occurred just after an instrument anomaly (see the Data Release Note of Sector 4 for more information⁵), and is visible in Figure A.1 as the first gap, which is noticeably bigger than the others. Finally, we normalized the four sectors by dividing each of them by their respective median flux and combined them into one light curve.

Appendix A.2: Identification of possible transit events

Sector 5 saw an automated creation of a Data Validation (DV) report, where the pipeline identified two decreases in brightness at about BTJD 1442 and BTJD 1459. They are marked by the leftmost two downward-pointing black arrows in Figure A.1. The third arrow is a clearly visible change in brightness for about two days at BTJD 1486. It is asymmetric in shape and very similar the the predicted light curve generated by a comet with an extended tail transiting the disk of the star, as hypothesised by Lecavelier Des Etangs et al. (1999). We used the apertures which were created by the pipeline visible as the white boxes in Figure A.2. The apertures have an elongated shape due to the blooming effect with a typical size of about 30 rows by 4 columns. To determine the robustness of these measurements, custom apertures of differing geometries were used to extract the photometry of β Pictoris - all three dips appear in these reductions. As a quick check, we used the TESScut function of lightkurve which allows us to create a light curve out of the Full Frame Images (FFIs). Those products are generated every 30 minutes by TESS. However, one has to consider that those - in contrast to the light curves provided by the pipeline - do not have an aperture mask and are not background corrected. After trying out different aperture masks and background masks for β Pictoris, we report that the dimming features are also distinctly visible in the FFIs.

We then inspected the postage stamp images, which have a cadence of 2 minutes. As the background is subtracted from the flux of the star, a bright object passing by - such as an asteroid - could temporarily increase the background flux and thus decrease the flux of the star. However, nothing like this is visible in the postage stamps during the dimming events. The times of the event do not coincide with momentum dumps (as can be seen in Figure A.1) and the jitter of TESS also did not increase.

We checked for similar dimmings in the stars closest to β Pictoris that have short cadence data. TIC 270574544 and TIC 270626557 have a separation of 810 and 1000 arcseconds relative to β Pictoris, which corresponds to 39 and 48 pixels respectively. Those two stars were observed in the same sectors as β Pictoris and on the same CCDs and no similar decrease in brightness is visible. Different background apertures in the vicinity of β Pictoris show no dips either. These last two checks also rule out a "rolling shutter" effect.

The brightest star besides β Pictoris in the pipeline aperture is Gaia DR2 4792773113918130560 in Sector 5 and Gaia DR2 4792772873399766528 in Sector 6 (Gaia Collaboration et al. 2016). Those stars are too faint to create those dimming events. Stars in the postage stamps of β Pictoris with a luminosity high enough to create those dips are marked with red circles in Figure A.2.

Finally we checked the possibility of Intra Camera Crosstalk as the cause of the dimmings. A bright object can create a decrease in flux in other parts of the same CCD (see §6.8.6 of

¹ https://mast.stsci.edu/portal/Mashup/Clients/Mast/
Portal.html

https://archive.stsci.edu/missions/tess/doc/TESS_ Instrument_Handbook_v0.1.pdf

https://archive.stsci.edu/tess/

⁴ https://archive.stsci.edu/missions/tess/doc/ EXP-TESS-ARC-ICD-TM-0014.pdf

⁵ https://archive.stsci.edu/tess/tess_drn.html

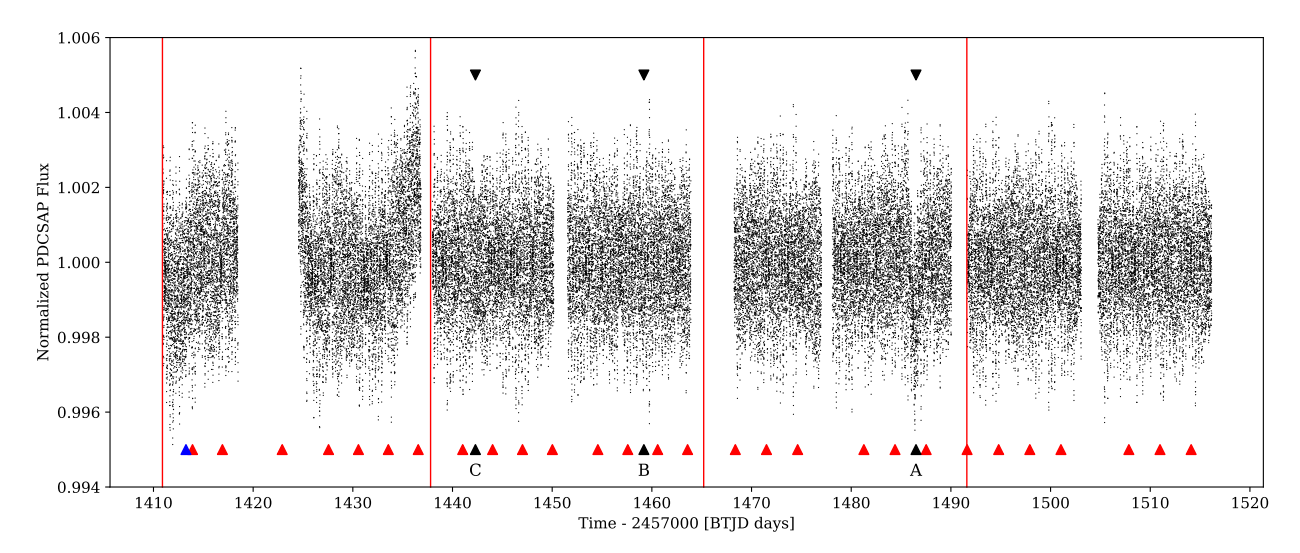


Fig. A.1. Full PDCSAP light curve of β Pictoris used in this analysis. The red vertical lines mark the starts of the Sectors 4 through 7. The black triangles point to the three identified decreases in flux, labelled A,B,C in decreasing signal to noise. The time of momentum dumps are marked with red triangles, and a small change in spacecraft pointing at the beginning of Sector 4 (due to an updated guide star table) with a blue triangle.

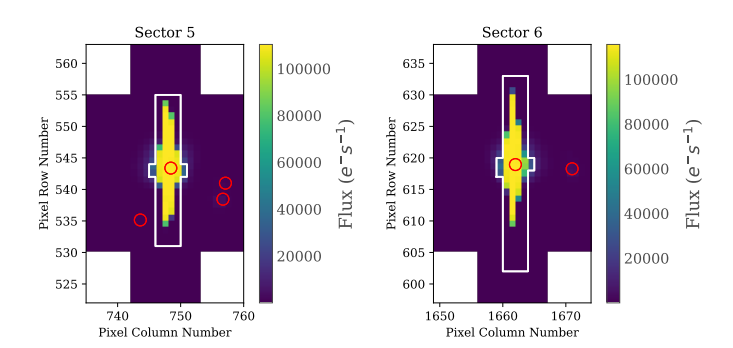


Fig. A.2. Postage stamps of β Pictoris for Sector 5 and 6. The stars which are bright enough to create such a dip in Sector 5 respectively 6 are marked with red circles. The white box is the pipeline aperture for those sectors. The only star in the aperture is in both cases β Pictoris.

the TESS Instrument Handbook⁶). Those echos can be found on the same row and 1024 columns higher than the bright source and they were only seen in CCD 3 of each camera. The big dip in Sector 6 was observed with CCD 3, however 1024 columns above β Pictoris lies outside the imaging area of this CCD.

We conclude that β Pictoris is the true host of the dimming events.

Appendix B: Details on the pulsation frequency analysis

For the pulsation frequency analysis we removed all Sector 4 data as the PDCSAP flux exhibits strong variations. As these are not visible in the SAP light curve, they are most likely artefacts of the reduction. Consequently, this part of the light curve would introduce artificial frequencies and, hence, was omitted for the pulsational analysis. The total time baseline of the TESS light curve used for the pulsational analysis is 78 days with a duty cycle of 80.5%.

The original amplitude spectrum of β Pictoris based on TESS data is shown in Figure B.1 where the detected pulsation frequencies are marked in red. The 54 δ Scuti-type frequencies, amplitudes and phases detected in the TESS data for β Pictoris are listed in Table B.1. Frequency, amplitude and phase errors are calculated using the relations by Montgomery & Odonoghue (1999). The zero-point for the phase calculation is at BTJD = 1410.9035 d.

⁶ https://archive.stsci.edu/missions/tess/doc/TESS_ Instrument_Handbook_v0.1.pdf

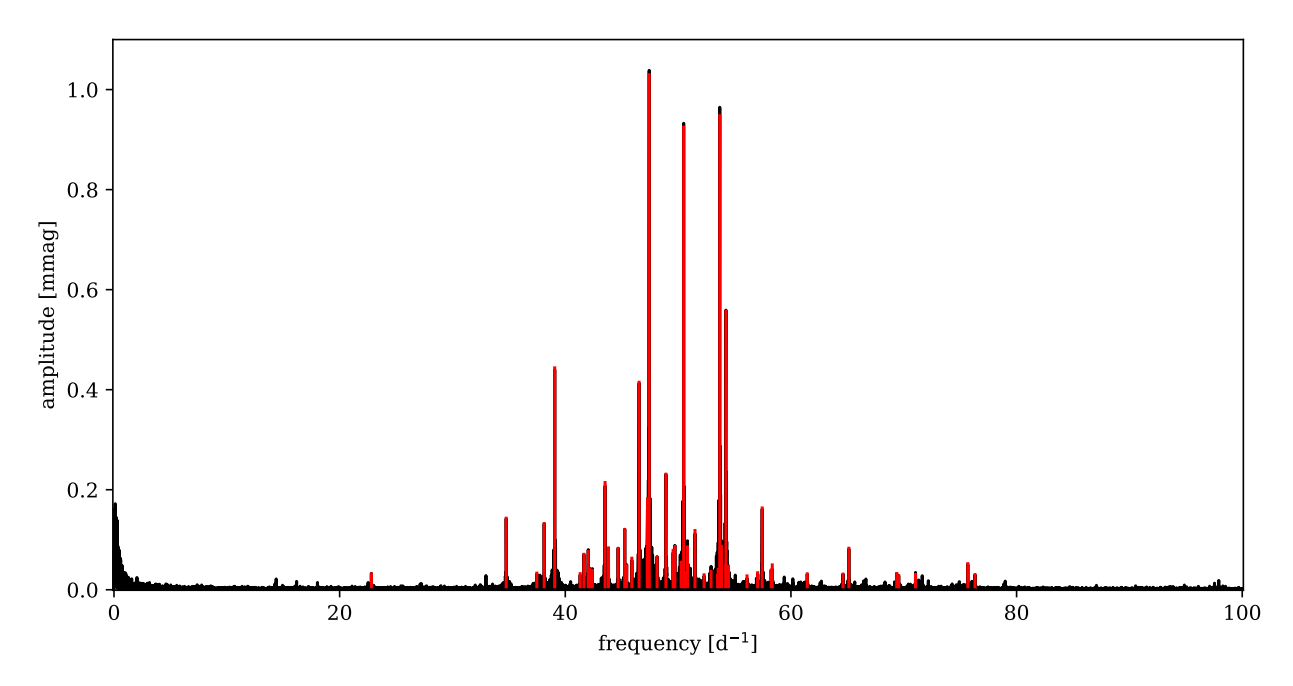


Fig. B.1. Pulsation frequency analysis of β Pictoris: The original amplitude spectrum is in black and the 54 identified δ Scuti pulsations are marked in red.

Table B.1. Pulsational frequencies, amplitudes, phases and signal-tonoise values sorted by the prewhitening sequence. Last-digit errors in frequencies, amplitudes and phases are given in brackets.

#	Frequency [d ⁻¹]	Amplitude [mmag]	Phase	SNR
1	47.438928(12)	1.048(2)	0.9334(4)	34.3
2	53.691744(12)	1.048(2)	0.1797(4)	36.4
3	50.491833(13)	0.940(2)	0.3251(4)	39.6
4	54.23744(2)	0.568(2)	0.5686(7)	41.7
5	39.06304(3)	0.442(2)	0.8625(9)	40.4
6	46.54302(3)	0.442(2)	0.8623(9)	27.3
7	48.91878(5)	0.414(2)	0.7382(9)	19.1
	43.52779(6)			
8 9		0.217(2)	0.7506(18)	20.6
10	47.28386(7)	0.175(2)	0.284(2)	22.1
11	57.45209(8) 34.76041(9)	0.163(2)	0.203(2) 0.914(3)	27.0 37.4
12		0.143(2)		
	38.12911(9)	0.133(2)	0.789(3)	33.2
13	45.26957(10)	0.122(2)	0.705(3)	15.9
14	51.49625(11)	0.118(2)	0.327(3)	15.5
15	47.27019(12)	0.108(2)	0.111(4)	15.5
16	53.85463(14)	0.090(2)	0.419(4)	13.0
17	49.71250(16)	0.077(2)	0.218(5)	12.9
18	50.83102(15)	0.087(2)	0.612(4)	15.7
19	43.82885(15)	0.083(2)	0.068(5)	12.9
20	65.13492(15)	0.082(2)	0.288(5)	24.1
21	44.68340(15)	0.083(2)	0.151(5)	16.9
22	49.55926(16)	0.079(2)	0.297(5)	14.9
23	42.03524(16)	0.077(2)	0.173(5)	16.7
24	41.65028(17)	0.073(2)	0.850(5)	18.2
25	48.1378(2)	0.062(2)	0.744(6)	15.4
26	45.90034(20)	0.064(2)	0.896(6)	14.3
27	50.2686(2)	0.056(2)	0.228(7)	15.8
28	75.6781(2)	0.051(2)	0.416(8)	17.2
29	58.3472(3)	0.041(2)	0.117(9)	9.2
30	54.2283(2)	0.062(2)	0.411(6)	9.2
31	45.4369(3)	0.049(2)	0.910(8)	13.4
32	54.4625(3)	0.048(2)	0.198(8)	9.5
33	53.5523(3)	0.038(2)	0.143(10)	12.6
34	42.1729(3)	0.044(2)	0.557(9)	12.5
35	58.2512(3)	0.041(2)	0.309(9)	13.7
36	42.3960(3)	0.040(2)	0.16(1)	4.7
37	52.9223(3)	0.040(2)	0.54(1)	9.0
38	53.68985(7)	0.174(2)	0.607(2)	15.5
39	57.0484(4)	0.032(2)	0.928(12)	15.4
40	50.6455(4)	0.033(2)	0.050(12)	6.7
41	37.4786(4)	0.033(2)	0.636(11)	6.6
42	69.3752(4)	0.033(2)	0.357(12)	13.7
43	41.3189(4)	0.033(2)	0.422(12)	18.9
44	61.4461(4)	0.032(2)	0.434(12)	4.3
45	22.8145(4)	0.031(2)	0.946(12)	4.3
46	64.6154(4)	0.031(2)	0.763(13)	4.2
47	71.0441(4)	0.036(2)	0.705(13)	4.2
47 48	52.3034(4)	0.030(2)	0.010(11)	8.8
49 50	47.4101(4)	0.035(2)	0.914(11)	10.0
50	76.3167(4)	0.030(2)	0.898(13)	10.4
51	45.3553(4)	0.028(2)	0.307(14)	10.1
52	53.4991(4)	0.031(2)	0.764(12)	8.2
53	69.5526(5)	0.027(2)	0.687(14)	4.6
54	56.1099(5)	0.026(2)	0.005(15)	4.0

Article number, page 8 of 8